emerald PUBLISHING

International Journal of Structural In

Empirical Modeling of Stress Concentration Factors Using Artificial Neural Networks for Fatigue Design of Tubular T-joint Under In-Plane and Out-of-Plane Bending Moments

Journal:	*International Journal of Structural Integrity*
Manuscript ID	IJSI-03-2024-0043.R1
Manuscript Type:	Research Paper
Keywords:	Artificial neural network, stress concentration factor, fatigue design, In-plane bending, Out-of-plane bending, T-joint

Empirical Modeling of Stress Concentration Factors Using Artificial Neural Networks for Fatigue Design of Tubular T-joint Under In-Plane and Out-of-Plane Bending Moments

Abstract:

Purpose – Stress concentration factors (SCFs) are commonly used to assess the fatigue life of tubular T-joints in offshore structures. SCFs are usually estimated from parametric equations derived from experimental data and finite element analysis (FEA). However, these equations provide the SCF at the crown and saddle points of tubular T-joints only, while peak SCF might occur anywhere along the brace. Using the SCF at the crown and saddle can lead to inaccurate hotspot stress and fatigue life estimates. There are no equations available for calculating the SCF along the T-joint's brace axis under in-plane and out-of-plane bending moments.

Design/methodology/approach – In this work, parametric equations for estimating SCFs are developed based on the training weights and biases of an artificial neural network (ANN), as ANNs are capable of representing complex correlations. 1250 finite element simulations for tubular T-joints with varying dimensions subjected to in-plane bending moments and out-of-plane bending moments were conducted to obtain the corresponding SCFs for training the ANN.

Findings – The ANN was subsequently used to obtain equations to calculate the SCFs based on dimensionless parameters (α, β, γ and τ). The equations can predict the SCF around the T-joint's brace axis with an error of less than 8% and a root mean square error (RMSE) of less than 0.05.

Originality/value – Accurate SCF estimation for determining the fatigue life of offshore structures reduces the risks associated with fatigue failure while ensuring their durability and dependability. The current study provides a systematic approach for calculating the stress distribution at the weld toe and SCF in T-joints using FEA and ANN, as ANNs are better at approximating complex phenomena than typical data fitting techniques. Having a database of parametric equations enables fast estimation of SCFs, as opposed to costly testing and time-consuming FEA.

Keywords: T-joint; Artificial neural network; stress concentration factor; fatigue design; finite element analysis; In-plane bending; Out-of-plane bending

Nomenclature: D = chord diameter; d = brace diameter; T = chord thickness; t = brace thickness; θ = angle between the brace and the chord; L = chord length; ℓ =brace length; β = ratio of the diameter of brace and chord; γ = ratio of chord's diameter and twice chord's thickness; τ= ratio of brace thickness to chord thickness; α = ratio of twice the length of the chord to the diameter of the chord; α_b = ratio of twice the length of brace to the diameter of the brace; r= brace radius; t= brace thickness; SCF = stress concentration factors; ANN= Artificial neural network; FEA= Finite element analysis; DOE= Design of experiments; R^2 = Coefficient of determination; IPB= In-Plane bending, OPB= Out-of-Plane bending; i_{max} = maximum of original input data; i_{min} = minimum of original input data; o_{max} = maximum of SCF data used for training; o_{min} = minimum SCF training data; F=force applied on the top of the brace; AWS = The American Welding Society; IIW = International Institute of Welding; API= American Petroleum Institute; GA= genetic algorithm; $\sigma_{nominal\ stress} =$ Nominal brace stress applied on brace; $\sigma_{hotspot\ stress} =$ Maximum stress along the weld toe; FFNN = feed-forward neural network design; DNV= Det Norske Veritas; UEG = Underwater engineering group; HSS= Hotspot stress; CHS= Circular hollow sections; N= Fatigue load cycles; σ_1 , σ_2 = Stresses at extrapolation points; Bx; bias value; A(x)= activation function; hnx= Neurons in the hidden layer ipx=input parameters; WWx= ANN weights

1. INTRODUCTION

Offshore platforms are subjected to cyclic wave loads, which may lead to fatigue failure after a specific number of cycles [1]. Therefore, accurately assessing the fatigue life of offshore tubular joints is critical to ensure structural durability and safe operation [2]–[4]. These platforms are usually formed with circular hollow sections tubular segments.

Branching components, or braces, are welded to the main structure or chord, creating tubular joints, with the T-joint among the most used tubular joints. Figure 1 shows a T-joint with a circular brace welded at 90° to a main chord. Fatigue failure is the most prevalent form of failure in engineering structures [5], and the fatigue life assessment of each structural component of an offshore structure is part of the fatigue design process. As joints are the most critical components of offshore structures, their fatigue life has a significant impact on the fatigue life of the entire structure [2].

Additional hollow sections include hybrid CHS-SHS, CHS-RHS, and SHS-RHS hollow sections [6]–[10], as well as rectangular hollow sections (RHS) and square hollow sections (SHS). Because of their high bending strength, high strength-to-weight ratio, non-directional buckling, and low wave resistance, circular hollow sections are frequently used in offshore structures [11], [12].

The hotspot stress (HSS) refers to the highest stress around the weld toe and is an essential measure for calculating the fatigue life of offshore structures [13]–[15]. The HSS can be calculated using the stress concentration factor (SCF) and the nominal brace load. Once the HSS is determined, the number of load cycles (N) for the fatigue life can be calculated using the S-N curves specified in the design codes [16], [17]. Accurate SCF prediction leads to accurate HSS calculations. Several factors influence the SCF, including joint shape, applied load, weld size and type, and distance from the weld. Over the last fifty years, significant research efforts have been made to develop accurate parametric equations for SCF [18]–[24]. Calculating the accurate SCF for determining the fatigue life of offshore structures reduces the risks associated with fatigue failure while ensuring their durability and dependability.

Tubular joint fatigue performance is generally evaluated through experimentation and finite element analysis (FEA). Costly experimentation is typically conducted to verify the numerical model. Further analysis is performed using the FEA. Additionally, numerical equations derived from FEA are utilized. Mathematical equation modeling has seen improvements. However, incorporating complex nonlinear patterns into the SCF equations of tubular joints is uncommon. Although equations obtained from regression of FEA datasets based on statistical methods are simple, they produce imprecise SCF. Some research has brought attention to this matter; however, the efficiency of empirical modeling techniques has led to the development of inefficient empirical models [25], [26]. ANN outperforms statistical methods that rely on simple assumptions and can accurately estimate the SCF in offshore joints ~~and~~. The benefits of ANN include its capability to efficiently approximate universal functions, process data in parallel, and effectively handle nonlinearity [2]. The ANN model's dependability and accuracy are demonstrated by achieving the highest coefficient of determination (R^2) throughout the training, validation, and testing subsets [2]. The challenges faced by artificial neural networks (ANN) include the quality and accessibility of data, optimizing the ANN architecture for best performance, and the necessary processing resources [2]. ANN should be examined to improve the correlation between input variables and SCF.

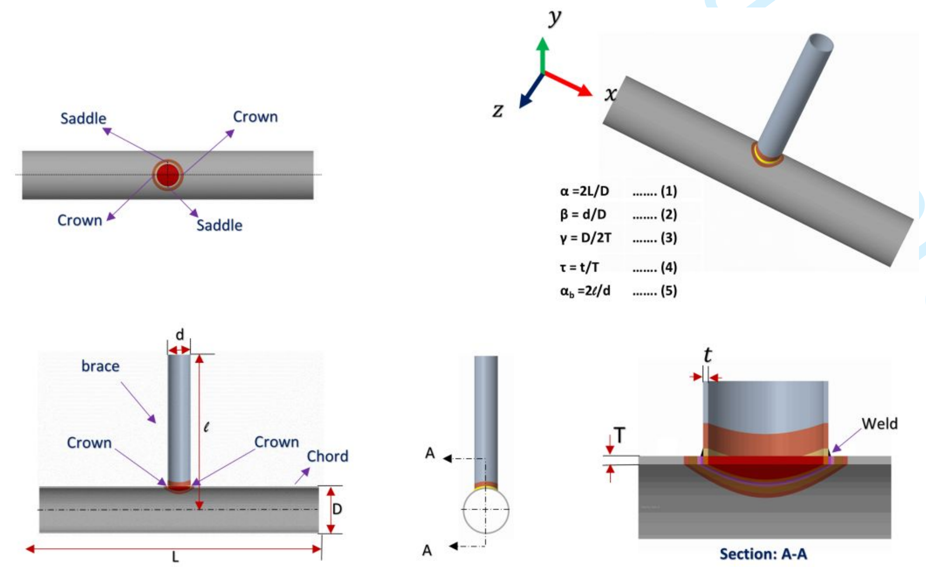

Where, D= Chord diameter, d= brace diameter, T= Chord thickness, t= brace thickness, L=chord length, ℓ = brace length

Figure 1: A typical Tubular T joint (Source: figure created by authors)

Offshore structures are subjected to multiaxial loading, a combination of axial and bending moments, because of the multidirectional character of sea states. As a result, the HSS can be situated anywhere around the intersection [27]. Following an examination of the impacts of member and load interaction, Gulati et al. [28] recommended that the HSS be derived by superimposing the stress distributions of all uni-axis load modes. The UEG [23] and the American Petroleum Institute (API) [29] recommend this method because it is the most precise and complete way to determine the stress distribution around the outer edge of the intersection [27]. However, this is rarely employed for T-joints due to limitations in existing parametric equations. The available models can only calculate SCFs at the crown and saddle position, while the maximum SCF may occur around the weld toe between the crown and saddle positions, which may result in an imprecise estimate of the HSS and the corresponding fatigue life [30].

Over the last 35 years, various parametric equations have been created to predict SCFs for tubular joints [18]–[24]. The UK Health and Safety Executive [20] report, released by Lloyd's Register, thoroughly evaluated the existing parametric equations for fundamental tubular junctions. These parametric equations were created by experimental study of specimens with tubular joints made of acrylic and steel. The Lloyd's Register (LR) equations [20] were derived by fitting the extracted SCF data to minimize the difference between the recorded and estimated SCF values at the saddle and crown points [4].

Smedley and Fisher [18] created parametric equations for single-plane joints (KT, Y, X, T, and K). These equations cannot be used to calculate the SCF along the weld line [4]. The Hellier, Connolly, and Dover (HCD) equations [19] were created to improve the precision of estimating the remaining lifespan of T/Y joints based on fracture mechanics concepts [3]. Nevertheless, they cannot account for the effects of every geometric parameter and may not provide sufficiently accurate findings for specific joints, as the equations were derived from a limited sample [27].

Efthymiou [24] provided a comprehensive mathematical formulae detailing KT, X, T, Y, and K joint designs. These formulae calculate the SCF at the crown and saddle points. They represent the average fit, leading to frequent underpredictions [20]. The equations created by Efthymiou [24] are currently used in ISO-19902 [31], as well as in the guidelines from DNV [32] and the API [29]. Linear regression equations usually give the SCF values at the saddle and crown positions. However, they might undervalue SCF if it is located between these positions. The Wordsworth/Smedley (W/S) equations [22] were developed using acrylic model test data for tubular junctions modeled without a weld fillet. Wordsworth's parametric equations focus on the saddle and crown positions. It is unclear whether intermediate positions were considered, particularly when the hot-spot stress is close to the saddle and crown [20]. Kaung et al. [21] developed parametric equations for SCF of KT, K, T, and Y joints using a finite element program. The Kuang equations were derived by statistical analysis of data collected from the examination of FE joints. The exact location of the hot-spot stress around the weld is not identified; instead, it is categorized as chord-side or brace-side. The equations fail to account for the impact of the chord length on the saddle caused by the constraints at the ends of the chord. Thus, it is probable that the SCFs for longer chord lengths (α) are underestimated due to Kuang's use of joints, mostly with shorter chord lengths [20].

The UEG [23] equations are based on the W/S and Wordsworth equations but include an adjustment for configurations with high γ (>20) and β (>0.6) values. Vinas-Pich [27] found that the UEG [23] stress distribution equations are not precise enough for the entire brace-chord junction. Haghpanahi et al. [33] numerically analyzed the T-joint under combined loading and found that the HSS is at the saddle position for axial loading and in the middle of the saddle and crown positions for combined loading; however, no mathematical equations were presented by the authors.

While stress distribution along the weld path is crucial [2], [25], [34]–[36], most research has been devoted to estimating the SCF at the saddle and crown positions. Given that ANNs have proven to be an effective approximator of complex phenomena [37], [38], their application in the mathematical modeling of SCF at a T-joint weld line under in-plane bending moments (IPB) and out-of-plane bending moments (OPB) is examined in this paper. The FEA was verified based on published results. Once the validity of the numerical model was verified, ANSYS Workbench 2021 R1 [39] was utilized to simulate a dataset intended for the Design of Experiment (DoE). The resulting DoE dataset was then exported to MATLAB [40]. In MATLAB, a neural network was constructed utilizing the nntool program with dimensionless parameters (α, β, γ, τ) as input and the SCF as output. The trained model's weights and biases were used to generate mathematical equations to calculate the SCF of the T-joint. The SCF is computed by this model at each 15° angle about the brace axis.

2. Methodology

In the process of ANN-based mathematical modeling, input parameter bounds are first established, and design configurations are then created, followed by finite element analysis. Lastly, the equations are developed using the ANN's weights and biases. Figure 2 depicts a flowchart that illustrates this methodology. The design dataset was created by defining design variables commonly used in the offshore industry. The datasets were analyzed using FEA, and the outcomes were stored. The data was transferred to MATLAB [40] for neural network modeling. The empirical model was developed using the ANN weights and biases from MATLAB [40]. The following subsections provide a detailed explanation of these steps.

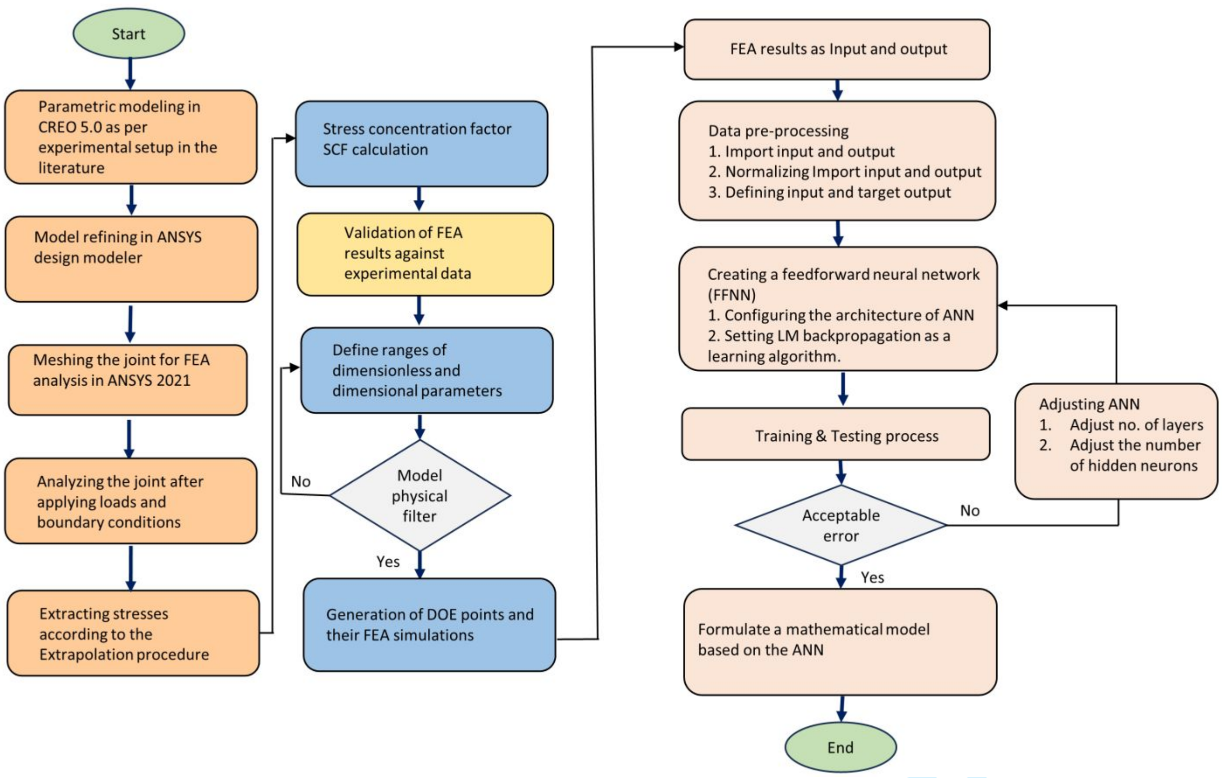

Figure 2: Methodology flowchart for ANN-based modeling of SCF (Source: figure created by authors)

2.1 **Finite element modeling**: CREO 5.0 [41] and ANSYS 2021 [39] were used for the finite element modeling of T-joints with dimensionless and dimensional parameters. DOE-based models were built using CREO 5.0 software [41] and refined in the ANSYS design modeler [39]. Linear elastic static analysis was performed in ANSYS 2021R1 [39], which is suitable for calculating SCFs in tubular joints [42].

2.1.1 **Parametric modeling in CREO 5.0.** The tubular T-joint was created in CREO 5.0 [41]. The model, as shown in Figure 1, was created using parametric equations, which utilized dimensionless and dimensional parameters outlined in Table 2 as variables. The parametric modeling allowed the fast and efficient update of the model to meet DOE requirements in seconds. Individual components were modeled and then joined, allowing sub-zone meshing, as seen in Figure 3.

2.1.2 **Weld profile:** The welding profile was examined to obtain an accurate SCF. The dimensions at the brace and chord connections are defined by the AWS D 1.1 standards [43], whereas the weld profile is designed as per the complete joint penetration (CJP) weld profiles [44] ~~as~~ in accordance with AWS D 1.1 [43], as detailed by Lotfollahi et al. [25]. Residual stresses were not considered as welded tubular connections in offshore constructions are post-heated after fabrication to reduce residual stresses caused by the welding process [45].

2.1.3 **Model refinement in Design Modeler**: The model was then imported into Design Modeler, where name selections were added, followed by model refinement.

2.1.4 **Material model:** The experimental coupon test results of the steel material by Ragupathi et al. [46] were the source of the material parameters for the brace and chord. The steel has a yield stress of 300 MPa, an ultimate stress of 415 MPa, Young's modulus of 207.9 GPa, and the Poisson's ratio of 0.29.

2.1.5 **Meshing:** Sub-zone meshing was selected for the parts at the brace and chord intersection. The coarser mesh was selected for brace and chord regions that are away from the brace and chord intersections. As shown in Figure 5, the extrapolation region was meshed to obtain nodes at 15° around the brace and to get nodes at extrapolation points (0.4T and 1.4T). As seen in Figure 3, the chord and brace were meshed separately, and ANSYS [39] contacts were used for their connections.

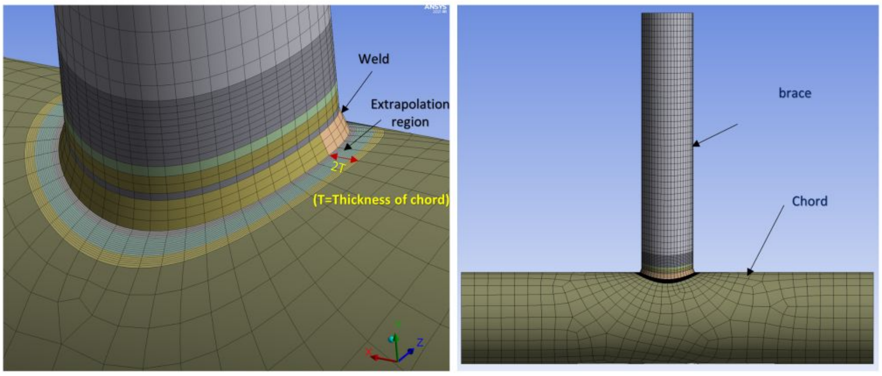

Figure 3: Mesh generated for FEA analysis of a T-joint in ANSYS 2021 [39] (Source: figure created by authors)

Before creating the FE models for the parametric analysis, a sensitivity assessment using various mesh densities was carried out to confirm the convergence of the FE data. ~~-~~Table 1 shows the results of sensitivity assessment. The FEA results of the sensitivity assessment was compared with the experimental results provided in Table 4. The sensitivity assessment led to the finalization of a mesh of 17728 elements.

Table 1: Mesh sensitivity assessment (Source: table created by authors)

Sr.No.	No. of elements	SCF_{crown} (FEA)	SCF_{saddle} (FEA)	SCF_{crown} FEA/ SCF_{crown} (Exp)	SCF_{saddle} FEA/ SCF_{saddle} (Exp)
1	11673	3.58	9.93	0.92	0.81
2	17728	3.67	10.69	0.94	0.88
3	22041	3.67	10.72	0.94	0.88

1.1.1 **Boundary conditions and Loads:** The load magnitudes were carefully selected to keep the deformation linearly elastic [47]. The ends of the chord were fixed, and a moment equivalent to 3 MPa stress was exerted at the top of the central brace. A moment equivalent to 3 MPa stress was chosen to ensure that the stresses in the weakest joint in the DoE remain under the elastic limit. The loads and boundary conditions are shown in the Figure 4.

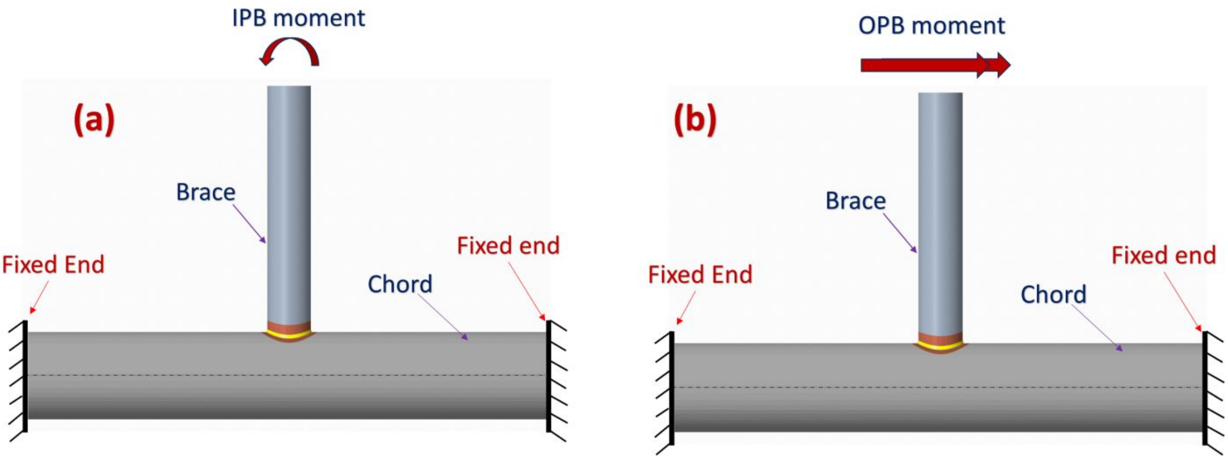

Figure 4: Loads and boundary conditions under (a) IPB moment (b) OPB moment (Source: figure created by authors)

1.1.2 **Extraction of stresses, extrapolation procedure and SCF calculation:** The SCF was determined using the IIW-XVE methodology developed by the International Institute of Welding [48]. The linear extrapolation of von Mises stresses was performed at two specific locations, 0.4T and 1.4T, from the weld toe, where T denotes the chord's thickness. Ahmadi et al. [34] and Hosseini et al. [49], [50] calculated the SCF using the von Mises stress. Due to the complex geometry of the weld toe, the SCF zone was divided into a separate mesh. The length of the SCF zone was set to twice the chord thickness so that the stress of the node at 1.4T from the weld toe was not affected by the coarser mesh beyond the extrapolation region and to obtain nodes at a distance of 0.1T from the weld toe. The area for extrapolation points near the brace was divided into 48 equal parts between 0˚ and 360˚ to measure stresses at 15˚ angle around the brace axis, as shown in Figure 5. The von Mises stresses were calculated for the fourth and fourteenth elements, and the hotspot stress at the weld toe was extrapolated accordingly. The SCF was calculated by dividing the stress at the hotspot by the nominal stress of the brace.

$$SCF = {}^{\sigma_{hotspot\ stress}}/_{\sigma_{nominal\ stress}} \ \ldots\ldots\ldots\ldots\ldots (6)$$

where,

$$\sigma_{hotspot\ stress} = 1.4\sigma_1 - 0.4\sigma_2 \qquad \ldots\ldots\ldots\ldots\ldots (7)$$

σ_1 and σ_2 are the stresses on the first and the second extrapolation points, respectively. The first and second extrapolation points are at 0.4*T and 1.4*T from the weld toe, respectively. The nominal stress, $\sigma_{nominal}$ can be calculated as follows.

$$\sigma_{nominal} = \frac{32dM}{\pi(d^4 - (\mathrm{d} - 2t)^4)} \qquad \ldots\ldots\ldots\ldots\ldots (8)$$

where M is the moment applied on the brace, d and t are the diameter and thickness of the brace (Figure 1), respectively.

The extrapolation points around the central brace, as recommended by the International Institute of Welding [48], are shown in Figure 5 below.

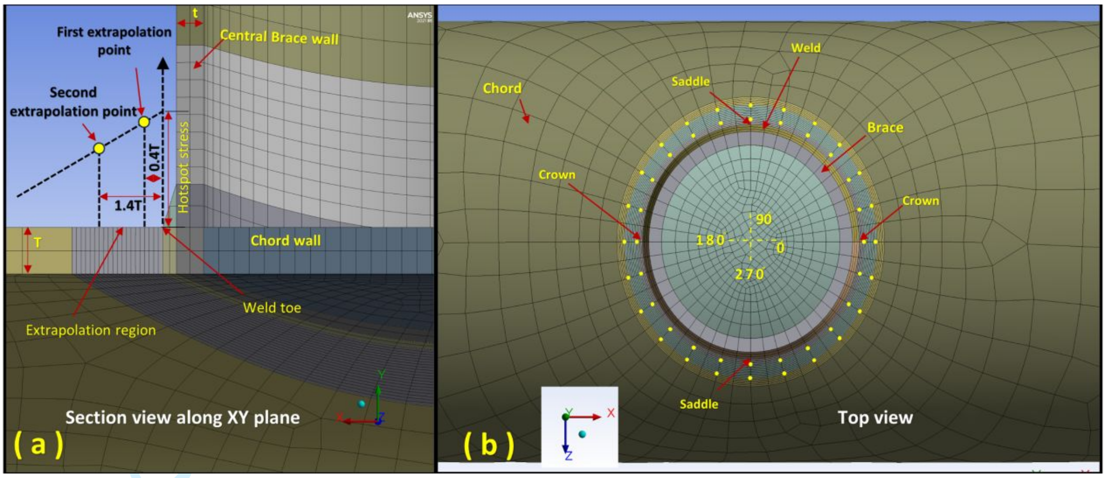

Figure 5: Extrapolation procedure as established by the International Institute of Welding IIW-XV-E-(1999) [48] (Source: figure created by authors)

Chang et al. [27] found that the brace length does not affect SCF when the ratio α_b (α_b =2 ℓ/d) exceeds a critical limit. Therefore, a brace length of ℓ=1000mm was chosen for all simulations.

1.1.3 **Determination of the specific values for the design parameters.** The design variables act as a function in the SCF equation. The ranges for design variables were chosen from their corresponding ranges commonly used in the offshore industry.

1.1.4 **Creation of the design's dataset.** The design dataset development was done in two stages. Initially, the entire range of geometric factors was considered in creating a set of design points. The dataset was then filtered based on the dimensionless parameters listed in Table 2. Because of its large size, the dataset was reduced for further study. A partial factorial design was used to limit the number of simulations, with five different values for each parameter.

2.2 Utilizing the MATLAB nntool for modeling with ANN. ANN is based on the universal approximation theory, which states that a basic neural network can approximate continuous functions based on given inputs [51]. The current study focused on creating an ANN model using FEA. The goal was to create new empirical formulas to determine the SCF of T-joints under IPB and OPB moment loads. The input data for MATLAB [40] comprised dimensionless parameters, with SCF as the output. The input and output data were imported into MATLAB's nntool module, and then a neural network was established. The Levenberg–Marquardt backpropagation algorithm was employed to implement supervised learning. This approach demonstrates increased efficiency due to its second-order convergence rate [2], [51]–[53] Figure 6 depicts a standard ANN model with an input layer containing two inputs, a hidden layer containing three neurons, and an output layer with two outputs.

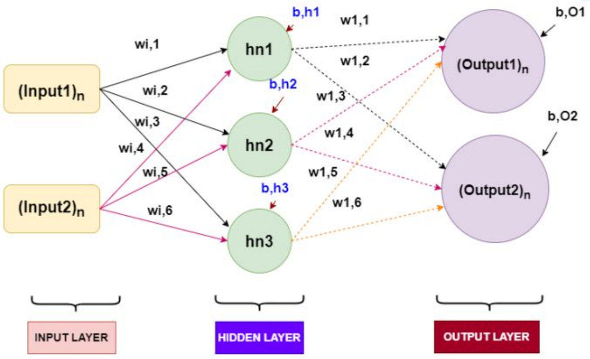

Figure 6: A typical feed-forward neural network (Source: figure created by authors)

The ANN underwent training using the specified input and output data. The hidden layers utilized tan-sigmoid, and the input and output layers utilized linear transfer functions, as described by Equations 9 and 10. The model's coefficient of determination (R^2) was used to assess the ANN's ability to create results that closely resembled the training data. The R^2 value, which represents the degree of correlation between the regression line of the ANN plot and the training data points, ranges from 0.0 to 1.0; a greater R^2 value implies a better fit.

$$a(x) = \frac{2}{(1+e^{-2x})-1} \qquad \dots\dots\dots\dots\dots\dots\dots\dots\dots \text{(9)}$$

$$\mathrm{f}(x) = x \qquad \dots\dots\dots\dots\dots\dots\dots\dots\dots \text{(10)}$$

2.2.1 Creation of an empirical model. The mathematical expressions of the trained ANN weights and biases were used to construct the equations. Equations 11 and 12 present the matrix representation of an ANN. Every neuron in the surrounding hidden layer (hnx) is linked to the inputs (ipx) with weights (WWx). The values are added after being multiplied by their respective weights. The sum of the products undergoes an activation function A(x), and the resulting output is then combined with a bias value (Bx). The neuron in the subsequent hidden layer takes input from the accumulated sum until the output layer.

$$\begin{bmatrix} hn1 \\ hn2 \end{bmatrix} = \begin{bmatrix} W1 & W3 & W5 \\ W2 & W4 & W6 \end{bmatrix} \begin{bmatrix} ip1 \\ ip2 \\ ip3 \end{bmatrix} + \begin{bmatrix} B1 \\ B2 \end{bmatrix} \qquad \dots\dots\dots\dots\dots\dots\dots\dots\dots \text{(11)}$$

$$[op] = \begin{bmatrix} W7 & W8 \end{bmatrix} \begin{bmatrix} hn1 \\ hn2 \end{bmatrix} + [B3] \qquad \dots\dots\dots\dots\dots\dots\dots\dots\dots \text{(12)}$$

2. Results and Discussion

Determination of the specific values for the design parameters. The T-joint's geometry is defined by dimensionless and dimensional features shown in Figure 1. The set of dimensionless and dimensional parameters and their ranges were selected to build a dataset for the DoE according to the established criteria in the offshore sector [3], [4], [20], [26], [54], [55]. Table 2 displays the range of these variables. 1250 design points were utilized in the simulation dataset.

Table 2: Parameters and their ranges (Source: Table created by authors)~~.~~

Sr.No.	Type of parameter	Parameter	Range	References
1	Dimensionless	α	8-40	[3], [4], [20], [26], [54], [55]
2		β	0.3-0.7	
3		γ	12-28	
4		τ	0.4-1	
5	Dimensional	ϴ	90˚	
6		D	300mm	
7		ℓ	1000mm	

Validation of FEA results against experimental data. The T-joint JISSP 1.13 was chosen from the experimental test results in the HSE OTH 354 report [20] to validate the accuracy of the finite element analysis. The parameters associated with the geometry of the validation joint were identical to those of the experimental models and are presented in

Table *3*. Figure 1 contains the relevant notations and definitions (Equations 1-5).

Table 3: Chord diameter and the other geometrical parameters of the validation joint (Source: table created by authors)

Reference joint	D (mm)	α	β	γ	τ
JISSP joint 1.13 [20]	508	6.2	0.8	20.3	1.07

The accuracy of the FEA findings was verified through a direct comparison with the experimental data published in JISSP1.13 tubular T-joints [20].

Table **4** summarizes the validation process by comparing the FEA results with the experimental results [20], API [29] and LR equations [20] at the saddle and crown positions. The values %error1, %error2 and %error3 in

Table **4** indicates the percentage discrepancy between the experimental results and the results obtained from the present study, API equations [29], and LR equations [20], respectively. The percentage error of present study was -5.90% for IPB moment and -12.46% for OPB moment load cases, demonstrating that the finite element model effectively predicts the SCF at the crown and saddle, and the SCF predictions are consistent with the test results.

Table 4: Validation of FEA results against experimental test results [20], API [29] and LR equations [20] (Source: table created by authors)

Joint	Position	Test results	Present study	API	LR	% Error1	% Error2	% Error3
JSIIP1.13	IPB (Crown)	3.90	3.67	4.85	4.07	-5.90	24.36	4.36
	OPB (Saddle)	12.20	10.68	15.29	14.11	-12.46	25.41	15.66

Creation of the design's dataset. After the FE model was validated, the design dataset simulations were carried out with CREO 5.0 [41], ANSYS [39], a Python script, and MATLAB [40]. Stress values were obtained at 15° around the brace's axis using a Python script in ANSYS Mechanical [39], and von Mises stresses at 0.4T and 1.4T were calculated. These stresses were then extrapolated to calculate the hot-spot stress at the weld toe. Linear stress extrapolation was chosen over nonlinear extrapolation due to the minimal difference in stress variation, which was less than 10% [20]. The hot-spot stress at the weld toe was extrapolated using the approach outlined in the International Institute of Welding IIW-XV-E-(1999) [48]. The SCFs were derived from the hotspot stress values using Equation 6 and then utilized to train the ANN. 1250 design configurations were successfully processed to provide outputs. Each cycle defined twenty-four output parameters, namely the SCF, at every 15° interval for a total of 360°.

Utilizing the MATLAB nntool for modeling with ANN. ANN training was conducted with a dataset comprising 1250 simulated design points. IPB and OPB have 625 design points each. An ANN model was created with dimensionless parameters (α, β, γ, τ) as input and SCF at a 15° offset as output. A feed-forward neural network (FFNN) design was used, consisting of an input layer, one or more hidden layers, and an output layer. During the training process, 70% of the design dataset was allotted to training, with validation and testing each receiving 15%.

Figure 7 (a & b) shows the architecture of the created ANN models for IPB and OPB, respectively. The neural network's ideal configuration was determined iteratively by altering the total number of hidden layers and hidden neurons through trial and error [37]. An ANN was built using one input layer, one hidden layer, and one output layer. The hidden layer consists of eight neurons for IPB and ten neurons for OPB load cases.

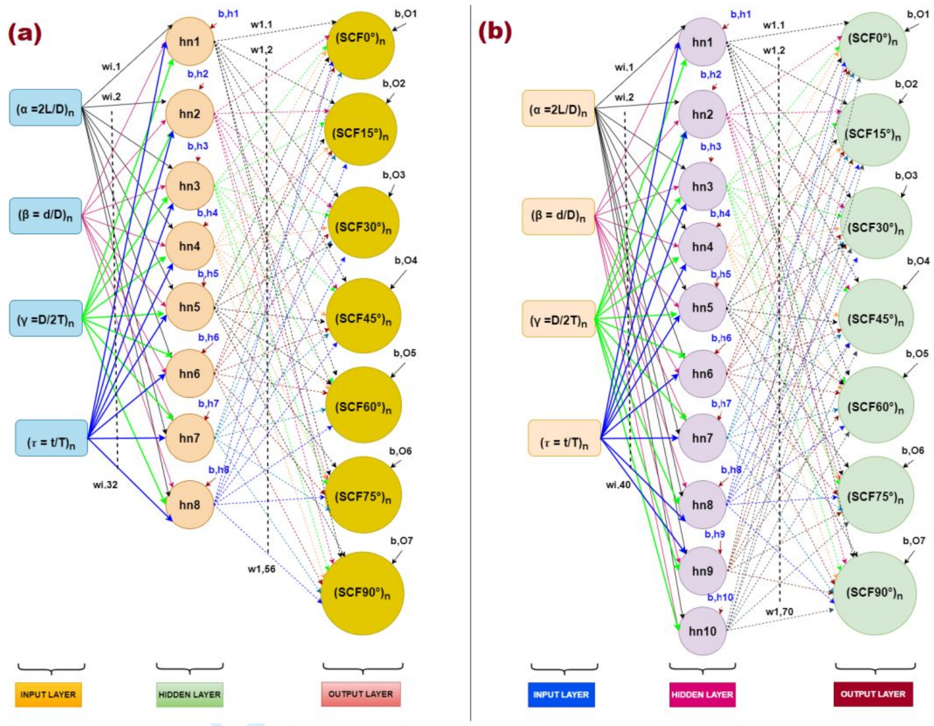

Figure 7: (a) The developed ANN (IPB) (b) The developed ANN (OPB) (Source: figure created by authors)

Figure 8(a&b) shows the regression plots generated by MATLAB R2021 [40] for the ANN. Both diagrams comprise four plots, one each for training, validation, and testing, and three combined plots. The plots show the linear regression line of best fit, which depicts the relationship between the ANN output and the desired output value. The solid lines represent the line of best fit, whereas the dashed lines represent the ideal or perfect results. Figure 8(a&b) shows that the solid and dotted lines in each plot have virtually perfect overlap, indicating that the ANN can provide outputs similar to the training data. The ANN demonstrated great accuracy by achieving R^2 values of 0.999 for IPB and OPB moment load scenarios (Figure 8). This high R^2 value of 0.999 for IPB and OPB moment load cases indicates a strong correlation between the ANN SCF predictions and the SCF derived from FEA.

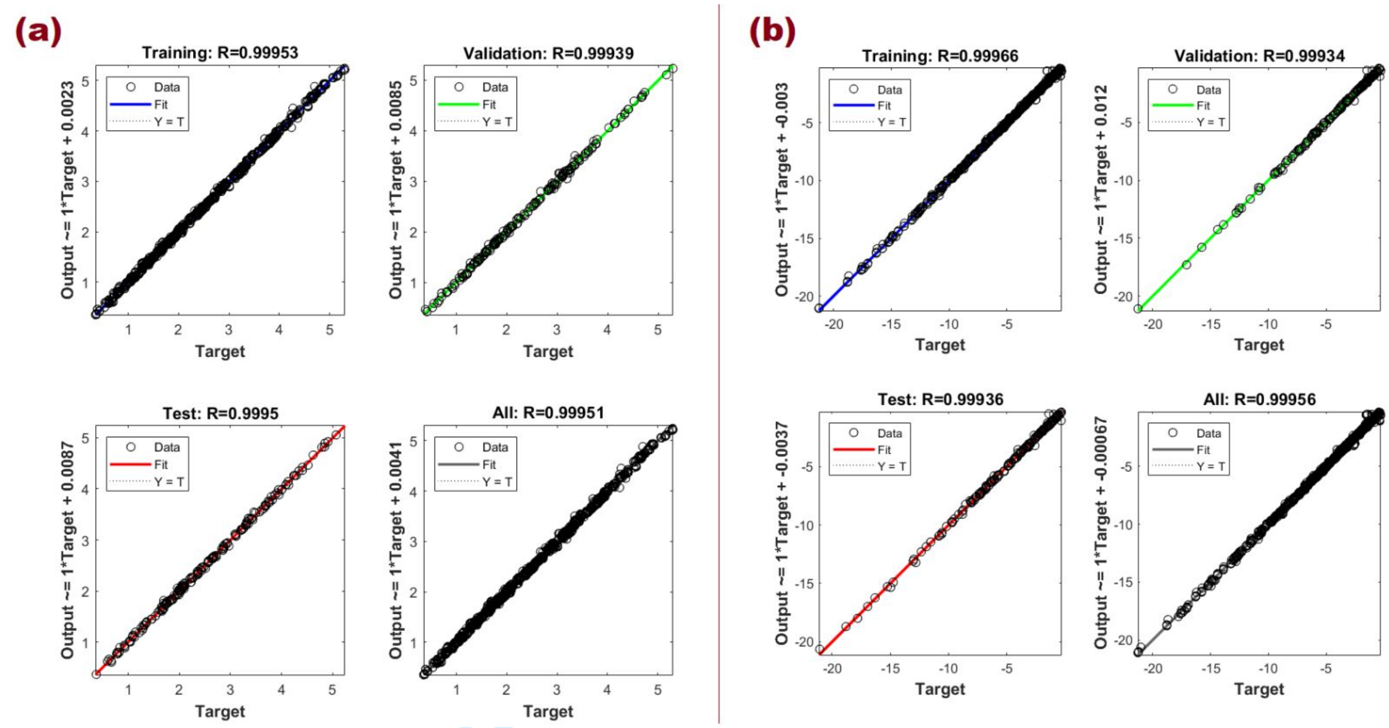

Figure 8: (a) Regression plot of trained ANN (IPB) (b) Regression plot of trained ANN (OPB) (Source: figure created by authors)

Figure 9(a&b) shows the performance graphs of the trained ANN during the validation process for IPB and OPB load cases, respectively. The best epoch yielded the weights for each neuron and biases for each layer, which were used for empirical modeling.

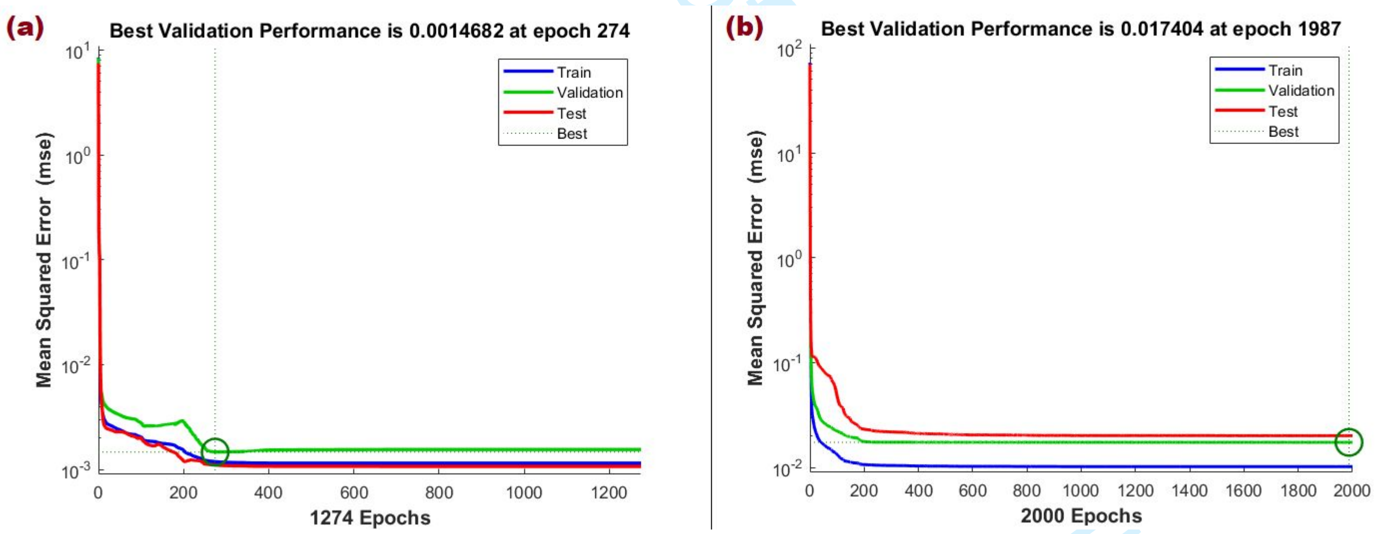

Figure 9: Performance validation of trained ANN (IPB) (b) Performance validation of trained ANN (OPB) (Source: figure created by authors)

Creation of an empirical model. The ANN's weights and biases were exported as a matrix. The inputs were normalized to prevent particular variables from dominating the result, and the outputs were denormalized. Normalization and denormalization can be achieved using Equations 11 and 12. Empirical formulas for SCFs are provided in Equations 13 and 14 for the IPB moment load case and in Equations 15 and 16 for the OPB moment load case.

$$i_{normalized} = i_{n,min} + \frac{(i_{n,max} - i_{n,min})(i - i_{min})}{(i_{max} - i_{min})} \quad \text{.. Equation 11}$$

$$o_{denormalized} = o_{min} + \frac{(o_n - o_{n,min})(o_{max} - o_{min})}{(o_{n,max} - o_{n,min})}$$ ……………………………………………. Equation 12

where, $i_{n,max}$ = 1 i_{max} = max of original input data

$i_{n,min}$ = -1 i_{min} = min of original input data

$o_{n,max}$ = 1 o_{max} = max of SCF data used for training

$o_{n,min}$ = -1 o_{min} = min of SCF data used for training

$$\begin{bmatrix} h1 \\ h2 \\ h3 \\ h4 \\ h5 \\ h6 \\ h7 \\ h8 \end{bmatrix} = \begin{bmatrix} 0.03 & 0.92 & 1.86 & -0.004 \\ -0.04 & -1.13 & -2.3 & -0.02 \\ -0.01 & 0.43 & 0.15 & -0.10 \\ 0.005 & 0.01 & 0.26 & 1.24 \\ -0.002 & 0.20 & 0.22 & 0.05 \\ 0.02 & 6.23 & 16.71 & 2.06 \\ 0.02 & -1.15 & 0.64 & 0.35 \\ 0 & 0.01 & 0.26 & -2.94 \end{bmatrix} \begin{bmatrix} \alpha_n \\ \beta_n \\ \gamma_n \\ \tau_n \end{bmatrix} + \begin{bmatrix} -0.45 \\ 0.43 \\ -0.10 \\ 1.28 \\ 0.16 \\ -13.67 \\ -1.86 \\ -0.90 \end{bmatrix}$$ ……………………………………………………………… Equation 13

$$\begin{bmatrix} SCF\ 0^\circ \\ SCF\ 15^\circ \\ SCF\ 30^\circ \\ SCF\ 45^\circ \\ SCF\ 60^\circ \\ SCF\ 75^\circ \end{bmatrix} = \begin{bmatrix} -2.02 & -1.58 & -2.20 & -1.30 & 5.08 & 0.14 & 0.06 & -0.70 \\ -1.69 & -1.31 & -2.27 & -1.39 & 5.18 & 0.11 & 0.01 & -0.74 \\ -0.83 & -0.63 & -2.40 & -1.62 & 5.28 & 0.03 & -0.12 & -0.84 \\ 0.25 & 0.21 & -2.39 & -1.79 & 5.03 & -0.03 & -0.26 & -0.91 \\ 1.44 & 1.14 & -2.41 & -2.02 & 4.73 & -0.09 & -0.38 & -1.02 \\ 2.50 & 1.99 & -2.38 & -2.15 & 4.35 & -0.13 & -0.49 & -1.07 \end{bmatrix} \begin{bmatrix} h1 \\ h2 \\ h3 \\ h4 \\ h5 \\ h6 \\ h7 \\ h8 \end{bmatrix} + \begin{bmatrix} -0.54 \\ -0.54 \\ -0.54 \\ -0.52 \\ -0.46 \\ -0.42 \end{bmatrix}$$ ……………………………………………… Equation

14

$$\begin{bmatrix} h1 \\ h2 \\ h3 \\ h4 \\ h5 \\ h6 \\ h7 \\ h8 \\ h9 \\ h10 \end{bmatrix} = \begin{bmatrix} 0.02 & -0.01 & 0.52 & 0.33 \\ -0.004 & 1 & 0.004 & -0.18 \\ 0.005 & 0.43 & 0.35 & 0.01 \\ 0.03 & 3.06 & 6.69 & 2.65 \\ -0.02 & -0.39 & -0.13 & -0.35 \\ -0.01 & -0.32 & -0.33 & -0.35 \\ -0.03 & 0.39 & 1.76 & 6.13 \\ -0.001 & -0.17 & -0.65 & 1.21 \\ 0.01 & 0.56 & 0.43 & -0.06 \\ 2.98 & -0.60 & -0.48 & -0.34 \end{bmatrix} \begin{bmatrix} \alpha_n \\ \beta_n \\ \gamma_n \\ \tau_n \end{bmatrix} + \begin{bmatrix} -1.11 \\ -0.34 \\ 0.16 \\ -6.21 \\ 1.58 \\ 1.22 \\ -4.78 \\ 1.28 \\ -0.03 \\ 4.46 \end{bmatrix}$$ …………………………………………………………………………… Equation 15

$$\begin{bmatrix} SCF\ 15^\circ \\ SCF\ 30 \\ SCF\ 45^\circ \\ SCF\ 60^\circ \\ SCF\ 75^\circ \\ SCF\ 90^\circ \end{bmatrix} = \begin{bmatrix} 0.21 & 0.62 & -2.17 & -0.07 & -2.06 & 0.84 & -0.18 & -0.50 & 0.73 & 0.21 \\ -1.35 & 0.08 & -3.69 & 0.10 & 0.53 & -1.11 & -0.05 & -0.18 & 3.14 & 0.58 \\ -0.80 & 0.67 & -3.03 & -0.09 & 3.53 & -3.9 & -0.17 & -0.49 & 1.32 & 0.31 \\ 0.05 & 0.77 & -2.31 & -0.08 & 0.62 & -0.80 & -0.17 & -0.54 & 0.41 & -0.10 \\ 0.63 & 0.53 & -1.49 & -0.003 & -2.99 & 3.03 & -0.08 & -0.36 & 0.19 & -0.36 \\ 0.75 & 0.39 & -1.28 & 0.02 & -4.15 & 4.17 & -0.04 & -0.27 & 0.28 & -0.40 \end{bmatrix} \begin{bmatrix} h1 \\ h2 \\ h3 \\ h4 \\ h5 \\ h6 \\ h7 \\ h8 \\ h9 \\ h10 \end{bmatrix} + \begin{bmatrix} 2.09 \\ -0.27 \\ -0.18 \\ 1.11 \\ 1.87 \\ 2.13 \end{bmatrix}$$ ……………………………………………… Equation 16

A dataset not part of the training, validation, or test data set was used to validate the empirical model. Table 5 displays six verification design points with their respective maximum absolute difference values, percentage differences, and Root Mean Square Errors (RMSE). Figure 10 (a&b) compares the SCF calculated using FEA in ANSYS Workbench [39] and ANN from the proposed empirical model.

Table 5: Verification results of the empirical model (Source: table created by authors)

Sr. No	**α**	**β**	**γ**	**τ**	**Max. absolute difference**		**Maximum % Error**		**RMSE (Route mean square error)**	
					IPB	**OPB**	**IPB**	**OPB**	**IPB**	**OPB**
1	8.40	0.56	12.90	0.72	0.04	0.14	4.86	3.37	0.00	0.01
2	15.90	0.31	19.80	0.68	0.12	0.10	5.21	5.65	0.01	0.00
3	8.10	0.49	15.60	0.95	0.05	0.30	1.71	5.09	0.00	0.03
4	32.50	0.66	23.80	0.75	0.12	0.26	6.99	5.03	0.02	0.03
5	39.70	0.52	15.50	0.89	0.03	0.42	1.29	7.20	0.00	0.05
6	15.70	0.68	27.50	0.95	0.09	0.36	1.87	6.72	0.00	0.03

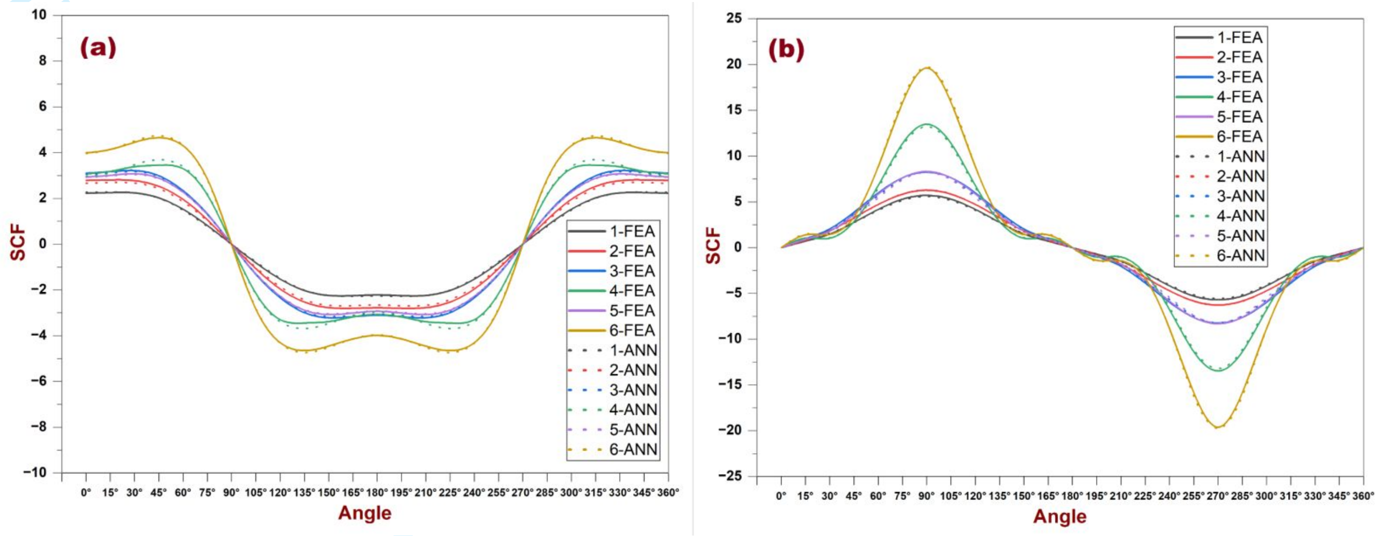

Figure 10: Comparison of ANN and FEA results for (a) IPB load cases and (b) OPB load cases (Source: figure created by authors)

The derived equations provide a precise estimation of the SCF quickly, with an error percentage of under 8% and an RMSE of less than 0.05 when compared to the SCF calculated via FEA. Hence, these equations can be utilized to calculate the SCF along the axis of the brace in a T-joint under IPB and OPB moment load conditions.

CONCLUSIONS

1. The equations established using ANN are efficient for estimating SCF in tubular joints. The integration of FEA and ANN has proven to be effective in estimating SCF. The equations can estimate the SCF around the T-joint's weld toe under IPB and OPB moment load cases with a percentage error of less than 8% and a root mean square error (RMSE) of less than 0.05. These equations remain applicable even when the maximum SCF position changes from the saddle or crown position.

2. Engineers in practice can utilize the equations (Equations 13-16) to calculate hotspot stress precisely and quickly, reducing the hazards associated with fatigue failure of offshore structures and ensuring their longevity and reliability. Our study helps to improve the safety and reliability of offshore structures by allowing for more exact estimates of stress distribution.

3. A similar approach can be used to compute SCF on the tubular joint's inclined braces. This approach can also be extended to other types of joints under different loading conditions to generate a set of equations for efficient SCF computations.

Funding

This research received funding from Yayasan Universiti Teknologi PETRONAS under grant No. 015LC0-443.

REFERENCES:

[1] X. Liu and M. Ma, “Cumulative fatigue damage theories for metals: review and prospects,” *Int. J. Struct. Integr.*, vol. 14, no. 5, pp. 629–662, 2023, doi: 10.1108/IJSI-09-2022-0119.

[2] A. Rasul, S. Karuppanan, V. Perumal, M. Ovinis, and M. Iqbal, “An artificial neural network model Tubular concentration factors for fatigue design of tubular T-joint under compressive loads,” *Int. J. Struct. Integr.*, no. 015, 2024, doi: 10.1108/IJSI-02-2024-0034.

[3] H. Ahmadi, M. Ali Lotfollahi-Yaghin, S. Yong-Bo, and M. H. Aminfar, “Parametric study and formulation of outer-brace geometric stress concentration factors in internally ring-stiffened tubular KT-joints of offshore structures,” *Appl. Ocean Res.*, vol. 38, pp. 74–91, 2012, doi: 10.1016/j.apor.2012.07.004.

[4] H. Ahmadi and E. Zavvar, “Stress concentration factors induced by out-of-plane bending loads in ring-stiffened tubular KT-joints of jacket structures,” *Thin-Walled Struct.*, vol. 91, pp. 82–95, 2015, doi: 10.1016/j.tws.2015.02.011.

[5] M. Ma, X. Liu, X. Yu, and X. Wang, “Fatigue life prediction for notched specimen considering modified critical plane method,” *Fatigue Fract. Eng. Mater. Struct.*, vol. 46, Dec. 2022, doi: 10.1111/ffe.13917.

[6] D. L. Chandramohan, K. Roy, H. Taheri, M. Karpenko, Z. Fang, and J. B. P. Lim, “A State of the Art Review of Fillet Welded Joints,” *Materials (Basel).*, vol. 15, no. 24, pp. 1–31, 2022, doi: 10.3390/ma15248743.

[7] R. Feng, C. Tang, K. Roy, Z. Chen, B. Chen, and J. B. P. Lim, “An experimental study on stress concentration factors of stainless steel hybrid tubular K-joints,” *Thin-Walled Struct.*, vol. 157, no. September, p. 107064, 2020, doi: 10.1016/j.tws.2020.107064.

[8] R. Feng, L. Chen, Z. Chen, B. Chen, K. Roy, and J. B. P. Lim, “Experiments on stainless steel hybrid K-joints with square braces and circular chord,” *J. Constr. Steel Res.*, vol. 185, no. August, p. 106865, 2021, doi: 10.1016/j.jcsr.2021.106865.

[9] R. Feng, C. Tang, Z. Chen, K. Roy, B. Chen, and J. B. P. Lim, “A numerical study and proposed design rules for stress concentration factors of stainless steel hybrid tubular K-joints,” *Eng. Struct.*, vol. 233, no. June 2020, p. 111916, 2021, doi: 10.1016/j.engstruct.2021.111916.

[10] R. Feng, J. Xu, Z. Chen, K. Roy, B. Chen, and J. B. P. Lim, “Numerical investigation and design rules for stress concentration factors of stainless-steel hybrid tubular joints,” *Thin-Walled Struct.*, vol. 163, no. April, p. 107783, 2021, doi: 10.1016/j.tws.2021.107783.

[11] D. S. Saini, D. Karmakar, and S. Ray-Chaudhuri, “A review of stress concentration factors in tubular and non-tubular joints for design of offshore installations,” *J. Ocean Eng. Sci.*, vol. 1, no. 3, pp. 186–202, 2016, doi: 10.1016/j.joes.2016.06.006.

[12] H. Nassiraei, M. A. Lotfollahi-Yaghin, and H. Ahmadi, “Static strength of offshore tubular T/Y-joints reinforced with collar plate subjected to tensile brace loading,” *Thin-Walled Struct.*, vol. 103, pp. 141–156, 2016, doi: 10.1016/j.tws.2016.02.010.

[13] X. Xu, Y. Shao, X. Gao, and H. S. Mohamed, “Stress concentration factor (SCF) of CHS gap TT-joints reinforced with CFRP,” *Ocean Eng.*, vol. 247, no. January, p. 110722, 2022, doi: 10.1016/j.oceaneng.2022.110722.

[14] S. Petinov and R. Guchinsky, “Criteria for Fatigue Failure of Materials: Application in Fatigue Assessment of Structures,” *Adv. Eng. Forum*, vol. 26, pp. 1–8, 2018, doi: 10.4028/www.scientific.net/aef.26.1.

[15] J. Wardenier, Y. Kurobane, J. A. Packer, G. J. Van der Vegte, and X.-L. Zhao, *Design guide for circular hollow section (CHS) joints under predominantly static loading*. Cidect, 2008.

[16] H. Nassiraei and P. Rezadoost, "Stress concentration factors in tubular T/Y-joints strengthened with FRP subjected to compressive load in offshore structures," *Int. J. Fatigue*, vol. 140, no. May, p. 105719, 2020, doi: 10.1016/j.ijfatigue.2020.105719.

[17] J. Lai, Y. Wang, Y. Wei, J. Liang, and X. Liu, "The prediction of residual life of liquid-storage tank considering the tank wall surface state," *Int. J. Struct. Integr.*, vol. 13, no. 6, pp. 985–998, 2022, doi: 10.1108/IJSI-05-2022-0070.

[18] P. Smedley and P. Fisher, "Stress concentration factors for simple tubular joints," in *ISOPE International Ocean and Polar Engineering Conference*, 1991, p. ISOPE-I.

[19] A. K. Hellier, M. P. Connolly, and W. D. Dover, "Stress concentration factors for tubular Y- and T-joints," *Int. J. Fatigue*, vol. 12, no. 1, pp. 13–23, 1990, doi: 10.1016/0142-1123(90)90338-F.

[20] HSE, "OTH 354 (1997) Stress Concentration Factors for Simple Tubular Joints-Assessment of Existing and Development of New Parametric Formulae," *Prep. by Lloyd's Regist. Shipp. UK*.

[21] J. G. Kuang, A. B. Potvin, and R. D. Leick, "Stress Concentration in Tubular Joints," *Offshore Technology Conference*. p. OTC-2205-MS, May 04, 1975. doi: 10.4043/2205-MS.

[22] A. C. Wordsworth and G. P. Smedley, "Stress concentrations at unstiffened tubular joints," in *European Offshore Steels Research Seminar[Proc. Conf.]*, 1978.

[23] U. E. G. (UEG), "Design of tubular joints for offshore structures," *UEG Publ.*, vol. 2, pp. 43–60, 1985.

[24] Mjrd. Efthymiou, "Development of SCF formulae and generalised influence functions for use in fatigue analysis." OTJ, 1988.

[25] M. A. Lotfollahi-Yaghin and H. Ahmadi, "Effect of geometrical parameters on SCF distribution along the weld toe of tubular KT-joints under balanced axial loads," *Int. J. Fatigue*, vol. 32, no. 4, pp. 703–719, 2010, doi: 10.1016/j.ijfatigue.2009.10.008.

[26] H. Ahmadi and M. A. Lotfollahi-yaghin, "Experimental and Numerical Investigation of Geometric SCFs in Internally Ring-Stiffened Tubular KT-Joints of Offshore Structures," *J. Persian Gulf*, vol. 43, no. 1, pp. 7–8, 2013, [Online]. Available: http://jpg.inio.ac.ir/files/site1/user_files_c8faec/admin-A-10-1-79-4c653d4.pdf

[27] E. Chang and W. D. Dover, "Parametric equations to predict stress distributions along the intersection of tubular X and DT-joints," *Int. J. Fatigue*, vol. 21, no. 6, pp. 619–635, 1999, doi: 10.1016/S0142-1123(99)00018-3.

[28] K. C. Gulati, W. J. Wang, and D. K. Y. Kan, "An Analytical Study of Stress Concentration Effects in Multibrace Joints Under Combined Loading," *Offshore Technology Conference*. p. OTC-4407-MS, May 03, 1982. doi: 10.4043/4407-MS.

[29] A. P. I. RP2A-WSD, "Recommended practice for planning, designing and constructing fixed offshore platforms–working stress design–," *Twenty-2000*, 2000.

[30] M. Iqbal, S. Karuppanan, V. Perumal, M. Ovinis, and H. Nouman, "analysis and artificial neural networks for the fatigue design of tubular KT- Empirical modeling of stress concentration factors using finite element analysis and artificial neural networks for the fatigue design of tubular KT-joints under combined loadin," no. August, 2023, doi: 10.1111/ffe.14122.

[31] N. ISO 19902, "Petroleum and natural gas industries—Fixed steel offshore structures," *Int. Organ. Stand.*, 2007.

[32] G. L. Dnv, "DNVGL-RP-C203: Fatigue design of offshore steel structures," *DNV GL, Oslo, Norw.*, 2016.

[33] M. Haghpanahi and H. Pirali, "Hot Spot Stress Determination for a Tubular T-Joint under Combined Axial and Bending Loading," *Int. J. Eng. Sci.*, vol. 17, no. 3, pp. 21–28, 2006.

[34] H. Ahmadi, M. A. Lotfollahi-Yaghin, and M. H. Aminfar, "Geometrical effect on SCF distribution in uni-planar tubular DKT-joints under axial loads," *J. Constr. Steel Res.*, vol. 67, no. 8, pp. 1282–1291, 2011, doi: 10.1016/j.jcsr.2011.03.011.

[35] E. Chang and W. D. Dover, "Stress concentration factor parametric equations for tubular X and DT joints," *Int. J. Fatigue*, vol. 18, no. 6, pp. 363–387, 1996, doi: 10.1016/0142-1123(96)00017-5.

[36] A. N'Diaye, S. Hariri, G. Pluvinage, and Z. Azari, "Stress concentration factor analysis for welded, notched tubular T-joints under combined axial, bending and dynamic loading," *Int. J. Fatigue*, vol. 31, no. 2, pp. 367–374, 2009, doi: 10.1016/j.ijfatigue.2008.07.014.

[37] M. Lo, S. Karuppanan, and M. Ovinis, "ANN-and FEA-Based Assessment Equation for a Corroded Pipeline with a Single Corrosion Defect," *J. Mar. Sci. Eng.*, vol. 10, no. 4, 2022, doi: 10.3390/jmse10040476.

[38] K. Miao, Z. Pan, A. Chen, Y. Wei, and Y. Zhang, "Machine learning-based model for the ultimate strength of circular concrete-filled fiber-reinforced polymer–steel composite tube columns," *Constr. Build. Mater.*, vol. 394, no. May, p. 132134, 2023, doi: 10.1016/j.conbuildmat.2023.132134.

[39] "Ansys Workbench | Simulation Integration Platform." [Online]. Available: https://www.ansys.com/products/ansys-workbench

[40] "R2021a - Updates to the MATLAB and Simulink product families - MATLAB & Simulink." [Online]. Available: https://www.mathworks.com/products/new_products/release2021a.html

[41] "Creo CAD Software: Enable the Latest in Design | PTC." [Online]. Available: https://www.ptc.com/en/products/creo

[42] A. N'Diaye, S. Hariri, G. Pluvinage, and Z. Azari, "Stress concentration factor analysis for notched welded tubular T-joints," *Int. J. Fatigue*, vol. 29, no. 8, pp. 1554–1570, 2007, doi: 10.1016/j.ijfatigue.2006.10.030.

[43] A. W. S. American Welding Society (2006), Structural Welding Code: AWS D 1.1, 24th ed.pp. 326-329, *Aws D1 .1/D1 .1 M:2020*. 2020.

[44] K. Hectors and W. De Waele, "Influence of weld geometry on stress concentration factor distributions in tubular joints," *J. Constr. Steel Res.*, vol. 176, 2021, doi: 10.1016/j.jcsr.2020.106376.

[45] A. Paradowska, J. Price, P. Dayawansa, B. Kerezsi, X.-L. Zhao, and R. Ibrahim, "Study of influence of post weld heat treatment on residual stress distribution in tubular joints," *Weld. Res. Abroad*, vol. 52, pp. 10–19, Jan. 2006.

[46] R. Masilamani and S. Nallayarasu, "Experimental and numerical investigation of ultimate strength of ring-stiffened tubular T-joints under axial compression," *Appl. Ocean Res.*, vol. 109, no. February, p. 102576, 2021, doi: 10.1016/j.apor.2021.102576.

[47] H. Ahmadi, M. A. Lotfollahi-Yaghin, and S. Yong-Bo, "Chord-side SCF distribution of central brace in internally ring-stiffened tubular KT-joints: A geometrically parametric study," *Thin-Walled Struct.*, vol. 70, pp. 93–105, 2013, doi: 10.1016/j.tws.2013.04.011.

[48] IIW-XV-E, "Recommended fatigue design procedure for welded hollow section joints." International Institute of Welding France, 1999.

[49] A. S. Hosseini, M. R. Bahaari, and M. Lesani, "SCF distribution in FRP-strengthened tubular T-joints under brace axial loading," *Sci. Iran.*, vol. 27, no. 3 A, pp. 1113–1129, 2020, doi: 10.24200/SCI.2018.5471.1293.

[50] A. Sadat Hosseini, M. R. Bahaari, and M. Lesani, "Stress concentration factors in FRP-strengthened offshore steel tubular T-joints under various brace loadings," *Structures*, vol. 20, no. July, pp. 779–793, 2019, doi: 10.1016/j.istruc.2019.07.004.

[51] S. Koric, A. Viswantah, D. W. Abueidda, N. A. Sobh, and K. Khan, "Deep learning operator network for plastic deformation with variable loads and material properties," *Eng. Comput.*, no. 0123456789, 2023, doi: 10.1007/s00366-023-01822-x.

[52] S. D. V. Kumar, S. Karuppanan, and M. Ovinis, "Failure pressure prediction of high toughness pipeline with a single corrosion defect subjected to combined loadings using artificial neural network (Ann)," *Metals (Basel).*, vol. 11, no. 2, pp. 1–25, 2021, doi: 10.3390/met11020373.

[53] F. S. Panchal and M. Panchal, "Review on Methods of Selecting Number of Hidden Nodes in Artificial Neural Network," *Int. J. Comput. Sci. Mob. Comput.*, vol. 3, no. 11, pp. 455–464, 2014, [Online]. Available: www.ijcsmc.com

[54] H. Ahmadi and M. A. Lotfollahi-Yaghin, "Stress concentration due to in-plane bending (IPB) loads in ring-stiffened tubular KT-joints of offshore structures: Parametric study and design formulation," *Appl. Ocean Res.*, vol. 51, pp. 54–66, 2015, doi: 10.1016/j.apor.2015.02.009.

[55] H. Ahmadi, A. Yeganeh, A. H. Mohammadi, and E. Zavvar, "Probabilistic analysis of stress concentration factors in tubular KT-joints reinforced with internal ring stiffeners under in-plane bending loads," *Thin-Walled Struct.*, vol. 99, pp. 58–75, 2016, doi: 10.1016/j.tws.2015.11.010.